Article | Open Access

Energy Materials

Zhao et al. Energy Mater. 2026, 6, 600025 DOI:10.20517/energymater.2025.202

Enhanced electrocatalytic Activity of NiCoP/Ni_5P_4@NiFe-LDH catalysts via Ir doping and oxygen vacancy engineering

Zhengxi Zhao[1,2,#], Liwei Sui[3,#], Ziqi Wang[2], Shiwei Song[2], Jian Wang[2], Yucai Li[2], Depeng Zhao[2], Guanglong Li[3], Lihua Miao[1,2,*]

Keywords:
Element doping, electrocatalyst, overall water splitting, hydrogen evolution reaction, oxygen evolution reaction

Citation: Zhao, Z.; Sui, L.; Wang, Z.; Song, S.; Wang, J.; Li, Y.; Zhao, D.; Li, G.; Miao, L. Enhanced electrocatalytic Activity of NiCoP/Ni_5P_4@NiFe-LDH catalysts via Ir doping and oxygen vacancy engineering. *Energy Mater.* **2026**, *6*, 600025. https://dx.doi.org/10.20517/energymater.2025.202

Received: 23 Nov 2025 **First Decision:** 24 Dec 2025 **Revised:** 21 Jan 2026 **Accepted:** 5 Feb 2026 **Published:** 17 Mar 2026

Academic Editor: Sining Yun
Copy Editor: Ping Zhang
Production Editor: Ping Zhang

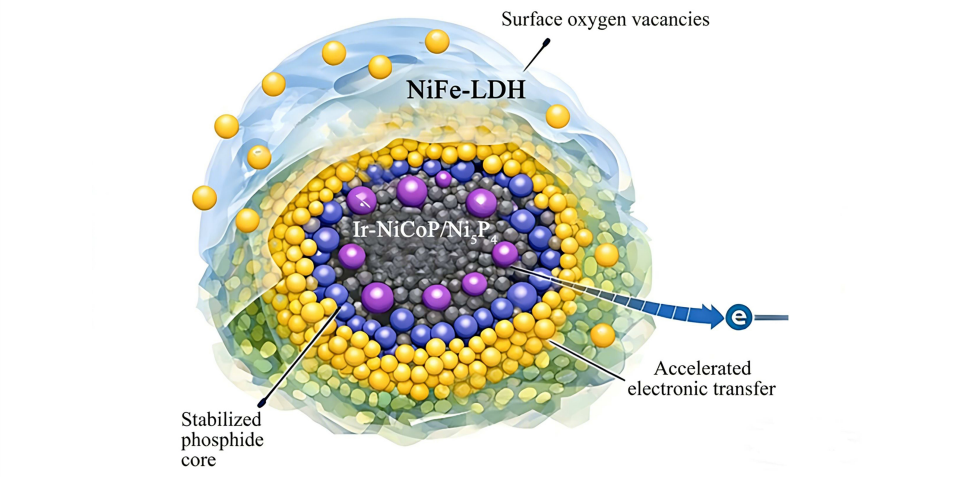

Abstract

Alkaline water electrolysis offers a promising route for large-scale hydrogen production, but its efficiency is limited by the sluggish kinetics of both the hydrogen evolution reaction (HER) and the oxygen evolution reaction (OER). Herein, we designed a hierarchical composite electrocatalyst comprising iridium-doped nickel-cobalt phosphide nanoparticles (Ir-NiCoP/Ni_5P_4) encapsulated within nickel-iron layered double hydroxide nanosheets (NiFe-LDH). Oxygen vacancies (O_V) were engineered on the surface via sodium borohydride reduction, yielding an optimized catalyst denoted as Ir-NiCoP/Ni_5P_4@NiFe-LDH-1-O_V. The optimized catalyst delivers low overpotentials of 52.7 mV for HER and 197.3 mV for OER at 10 mA cm^{-2} and maintains remarkable stability over 100 h for overall water splitting. Moreover, the Ir-NiCoP/Ni_5P_4@NiFe-LDH catalyst exhibits overpotentials of 76.7 and 101.3 mV for HER and the ammonia oxidation reaction A in 1 M KOH + $NH_3 \cdot H_2O$, respectively.

[1]School of Medical Information Engineering, Shenyang Medical College, Shenyang 110034, Liaoning, China.
[2]School of New Energy, Shenyang Institute of Engineering, Shenyang 110136, Liaoning, China.
[3]School of Materials Science and Engineering, Shenyang University of Technology, Shenyang 110870, Liaoning, China.
[#]Authors contributed equally.

[*]**Correspondence to:** Prof. Lihua Miao, School of Medical Information Engineering, Shenyang Medical College, Shenyang 110034, Liaoning, China. E-mail: miaolihua@symc.edu.cn

INTRODUCTION

Driven by the twin pressures of global energy scarcity and environmental degradation, the development of clean, renewable energy technologies has emerged as a critical imperative[1,2]. Among the promising candidates, hydrogen stands out as a carbon-neutral energy carrier with exceptionally high energy density[3,4]. Electrocatalytic water splitting offers a sustainable and efficient pathway for hydrogen production that can be seamlessly integrated with renewable electricity sources[5]. While noble-metal catalysts - particularly Pt for the hydrogen evolution reaction (HER) and RuO_2/IrO_2 for the oxygen evolution reaction (OER) - demonstrate benchmark performance, their prohibitive cost and scarcity severely constrain widespread commercial deployment[6]. These challenges underscore the urgent need to develop earth-abundant, cost-effective electrocatalysts that combine high catalytic activity with robust long-term stability[7,8].

Transition metal phosphides (TMPs) have attracted considerable interest as electrocatalysts owing to their high activity, stability, and low cost[9]. Filled d-orbitals flexible redox behavior and high electron-transfer capability, lowering activation barriers and thereby enhancing hydrogen production efficiency[10]. Numerous synthetic routes have been reported, including direct reactions between red phosphorus and transition metals, electrolysis in molten metal salts, reactions of metal halides with PH_3 or Na_3P, decomposition of organometallic precursors, and reduction of metal phosphates[11-15]. For example, Liu *et al.* prepared the NiCoP/Co_xP catalyst on nickel foam (NF) via electrodeposition followed by chemical vapor deposition (CVD), achieving an HER overpotential of 290 mV at 10 mA cm^{-2} and operating stably for 500 h at 10 mA cm^{-2} in seawater with excellent corrosion resistance[16]. Wu *et al.* produced a core-shell CoP_x@FeOOH/NF catalyst using a three-step hydrothermal-phosphidation-electrodeposition method, which necessitated 190 and 248 mV to achieve 100 and 500 mA cm^{-2}, respectively, while demonstrating exceptional durability for over 80 h in 1.0 M KOH seawater[17]. Despite these advances, pristine TMPs suffer from two critical limitations that hinder their practical application: (i) severe surface oxidation and phosphorus leaching under OER conditions, leading to gradual deactivation, and (ii) insufficient active site density and poor mass transport due to inevitable nanoparticle agglomeration. To overcome these challenges, constructing hierarchical composite architectures by integrating TMPs with layered double hydroxides (LDHs) has emerged as a promising strategy. LDHs play multifunctional roles: their 2D layered structure serves as a physical barrier against phosphorus leaching, tunable interlayer spacing facilitates ion diffusion, and abundant surface hydroxyl groups provide additional active sites for OER via a lattice-oxygen-mediated mechanism. Recent studies have demonstrated that strategic compositional engineering of LDH-based composites can significantly enhance OER performance[18]. For instance, Li *et al.* reported that atomically dispersed Ru doped into iron-nickel LDH forms an asymmetric Ru-Fe dipole that creates electron-deficient active sites, substantially accelerating OER kinetics and achieving an overpotential of only 230 mV at 10 mA cm^{-2} in 1 M KOH [19]. Similarly, Abdelghafar *et al.* demonstrated that cation nonstoichiometry in perovskite oxides can induce the formation of nanocomposites with strongly interacting phases, promoting a lattice-oxygen-participating OER pathway and achieving enhanced electrocatalytic performance through synergistic interfacial effects[20]. However, conventional physical mixing or weak interfacial contact in TMP/LDH composites often results in limited charge transfer efficiency across the heterojunction, compromising the synergistic potential. To rationally enhance interfacial coupling, precise electronic modulation through selective doping becomes essential. Among various dopants, Ir stands out - despite its high cost - because its unique 5d electronic configuration and moderate electronegativity enable exceptional charge redistribution capability. Critically, atomically dispersed Ir^{3+} can simultaneously stabilize both the TMP core through robust Ir-P bonds and the LDH shell via Ir-O-Fe bridges, forming an asymmetric Ir-Fe dipole that accelerates interfacial electron transfer.

In this work, core-shell structured NiCoP/Ni_5P_4 composites were subsequently coated with NiFe-LDH. Ir incorporation and $NaBH_4$-induced oxygen vacancy formation were further introduced to modulate the

electronic structure and increase the density of exposed active sites. The material exhibited outstanding HER and OER performance in 1 M KOH solution, as well as excellent ammonia oxidation reaction (AOR) performance in 1 M KOH + $NH_3 \cdot H_2O$ solution, demonstrating remarkable advantages including low overpotentials, low Tafel slopes, large electrochemical capacitance, and exceptional long-term cycling stability. Furthermore, it displayed superior electrocatalytic performance for efficient overall water splitting, achieving excellent long-term durability.

EXPERIMENTAL

Synthesis of the samples

All chemicals used in this experiment were purchased from Aladdin Reagent (Shanghai) Co., Ltd., with a purity of ≥ 96% and were used directly without further purification. They include nickel(II) nitrate hexahydrate [$Ni(NO_3 \cdot 6H_2O$], cobalt(II) nitrate hexahydrate [$Co(NO_3)_2 \cdot 6H_2O$], iron(III) nitrate nonahydrate [$Fe(NO_3) \cdot 9H_2O$], urea, ammonium fluoride (NH_4F), sodium hypophosphite monohydrate ($NaH_2PO_2 \cdot H_2O$), iridium(III) chloride ($IrCl_3$), sodium hydroxide (NaOH), sodium borohydride ($NaBH_4$), and hydrochloric acid (HCl). All reagents met the required purity standards, ensuring reaction stability and reproducibility. NF (4 cm × 4 cm) was sonicated sequentially in hydrochloric acid and ultrapure water (30 min each) to remove surface oxides. A precursor solution was prepared by dissolving $Ni(NO_3)_2 \cdot 6H_2O$ (1 mM), $Co(NO_3)_2 \cdot 6H_2O$ (1 mM), urea (6 mM), and NH_4F (2.5 mM) in 60 mL of deionized water. After 30 min of stirring, the solution and NF were transferred to a 100 mL stainless steel autoclave and hydrothermally treated at 120 °C for 6 h. The product was dried at 60 °C for 6 h. For phosphidation, the dried sample and $NaH_2PO_2 \cdot H_2O$ (5 g) were placed downstream and upstream, respectively, in a tube furnace and annealed at 350 °C for 2 h under Ar flow.

An aqueous precursor was prepared by dissolving $Ni(NO_3)_2 \cdot 6H_2O$ (1.5 mM), $Fe(NO_3)_3 \cdot 9H_2O$ (0.5 mM), urea (5 mM), and NH_4F (5 mM) in 60 mL of deionized water. The solution and the substrate obtained in step 1 were transferred to a 100 mL stainless steel autoclave and hydrothermally treated at 120 °C for 4 h, then allowed to cool and dried to yield the product. The procedure was repeated with the $Fe(NO_3)_3 \cdot 9H_2O$ concentration increased to 1.0 mM while keeping the other reagent concentrations unchanged, producing a second sample under identical conditions. Finally, the $Fe(NO_3)_3 \cdot 9H_2O$ concentration was increased to 1.5 mM, and the process was repeated to obtain a third sample.

Six milligrams of $IrCl_3$ were dissolved in 60 mL of 0.01 M NaOH and stirred for 20 min. The resulting solution and two samples prepared with 1.0 mM $Fe(NO_3)_3 \cdot 9H_2O$ were transferred to a 100 mL stainless steel autoclave and hydrothermally treated at 120 °C for 2 h. The product was then washed and dried. The as-prepared material was subsequently immersed in 100 mL of 1 mM $NaBH_4$ for 15 min, removed, thoroughly rinsed, and dried. Based on the $Fe(NO_3)_3 \cdot 9H_2O$ content, the samples were designated as NiCoP/Ni_5P_4, NiCoP/Ni_5P_4@NiFe-LDH-0.5, NiCoP/Ni_5P_4@NiFe-LDH-1, NiCoP/Ni_5P_4@NiFe-LDH-1.5, Ir-NiCoP/Ni_5P_4@NiFe-LDH-1, and Ir-NiCoP/Ni_5P_4@NiFe-LDH-1-O_V.

Structure characterization

Morphology and crystal structure were characterized by X-ray diffraction (XRD, Shimadzu XRD-7000, Cu Kα), X-ray photoelectron spectroscopy (XPS, Thermo ESCALAB 250, Al Kα), scanning electron microscopy (SEM, Zeiss Gemini 300-71-31), and transmission electron microscopy (TEM, JEOL JEM-2100 Plus).

RESULTS AND DISCUSSION

Figure 1A presents the XRD pattern of the synthesized material. The characteristic peaks observed at 2θ values of 40.78°, 44.72°, 47.66°, and 55.29° are attributed to the (111), (201), (210), and (211) planes of

hexagonal NiCoP/Ni_5P_4, respectively (JCPDS PDF No.71-2336). Additionally, the peaks at 2θ = 31.55°, 41.49°, 49.34°, and 52.26° correspond well to the (201), (211), (302), and (106) planes (JCPDS PDF No.18-0336). The peaks at 2θ = 19.98° and 22.21° are consistent with the (330) and (332) planes (JCPDS PDF No. 25-0608), respectively[21,22]. XPS was further performed to investigate the composition and elemental states of NiCoP/Ni_5P_4@NiFe-LDH-1 and Ir-NiCoP/Ni_5P_4@NiFe-LDH-1-O_V. Supplementary Figure 1 presents a comparison of the survey spectra for both materials, which clearly reveals the characteristic peaks of Ir, confirming the successful incorporation of Ir into the material. Supplementary Figure 2 shows the elemental composition of Ir-NiCoP/Ni_5P_4@NiFe-LDH-1-O_V, revealing the presence of Ni, Co, P, Ir, O, and C as the main elements, with contents of 11.47%, 3.03%, 3.2%, 3.12%, 47.77%, and 25.81%, respectively. Figure 1B-E illustrates the XPS spectra of the NiCoP/Ni_5P_4@NiFe-LDH-1 and Ir-NiCoP/Ni_5P_4@NiFe-LDH-1-O_V samples. Characterization of the NiCoP/Ni_5P_4@NiFe-LDH-1 material was shown, revealing that the Ni 2p spectrum consists of peaks at approximately 856.3 and 873.5 eV, corresponding to the Ni^{2+} $2p_{3/2}$ and $2p_{1/2}$ states, respectively [Figure 1B]. The peaks for Ni^{3+} $2p_{3/2}$ and $2p_{1/2}$ appear at binding energies of 858.2 and 875.5 eV, respectively, accompanied by two satellite peaks centered at 861.8 and 880 eV[23]. Furthermore, Figure 1C shows the Co 2p spectrum, where peaks at 782.98 and 797.88 eV are associated with Co^{2+} $2p_{3/2}$ and $2p_{1/2}$, while those at 780.1 and 795.78 eV correspond to Co^{3+} $2p_{3/2}$and $2p_{1/2}$. The peaks at 786.1 and 803.2 eV are indexed as satellite peaks[24]. In Figure 1D, two characteristic peaks at 714.82 and 725.84 eV, with a spin energy separation of 13.02 eV, are ascribed to Fe $2p_{3/2}$ and Fe $2p_{1/2}$, characteristic of Fe^{3+}. The peaks at binding energies of 717.16 and 728.30 eV are satellite peaks of Fe $2p_{3/2}$ and Fe $2p_{1/2}$, while those at 712.30 and 722.40 eV correspond to Fe^{2+}[25]. The peaks at 707.10 and 721.20 eV are attributed to the Fe-P bond formed by the reaction between Fe and P[26]. In the P 2p XPS spectrum [Supplementary Figure 3A], a prominent peak at 134.6 eV, attributed to P-O, is observed, primarily resulting from the formation of metal phosphides upon exposure to air. The peaks at 129.5 and 130.4 eV correspond to P $2p_{3/2}$ and P $2p_{1/2}$, respectively[27]. As shown in Supplementary Figure 3B, the peaks at 531.1 and 532.1 eV originate from the splitting of the O 1s peak. The peak at 531.1 eV is associated with oxygen vacancies[28], while the peak at 532.1 eV corresponds to adsorbed oxygen[29]. These peaks are attributed to metal hydroxides and metal carbonates, respectively. XPS analysis was performed to examine the structure after Ir doping. The spectral features of Ni, Co, P, O, and Fe elements remained essentially consistent with those of the pristine NiCoP/Ni_5P_4@NiFe-LDH material. As shown in Figure 1E, spin-orbit doublet peaks were observed at 62.40 and 65.30 eV, corresponding to Ir $4f_{7/2}$ and Ir $4f_{5/2}$, respectively, confirming the presence of Ir in the trivalent state. These results further validate the successful incorporation of Ir into the material. Electron paramagnetic resonance (EPR) spectroscopy provides direct evidence for oxygen vacancies and their concentration modulation in the catalysts. As shown in Figure 1F, all samples display a prominent symmetric signal at g = 2.003, indicating that the unpaired electrons are highly localized at oxygen-deficient sites with minimal spin-orbit coupling. It confirms that $NaBH_4$ reduction effectively introduces a higher concentration of surface-exposed oxygen vacancies.

SEM was utilized to clarify the microstructural properties of the materials. Figure 2A illustrates that the SEM images of NiCoP/Ni_5P_4@NiFe-LDH-1 exhibit a sheet-like shape on the material's surface. Following Ir incorporation, the modified NiCoP/Ni_5P_4@NiFe-LDH-1 displays a unique porous structure, as demonstrated by the SEM images in Figure 2B. This porous structure is anticipated to reveal numerous active sites during catalytic reactions, therefore improving catalytic efficacy. SEM images of Ir-NiCoP/Ni_5P_4@NiFe-LDH-1-O_V [Figure 2C] demonstrate that $NaBH_4$ treatment causes a significant morphological alteration, leading to a hierarchical spheroidal structure formed by interconnected nanosheets. This shape augments the density of available active sites, hence improving catalytic performance while maintaining intrinsic activity throughout extended cycling. The microstructural characteristics support the enhanced catalytic efficacy of Ir-NiCoP/Ni_5P_4@NiFe-LDH-1-O_V described below.

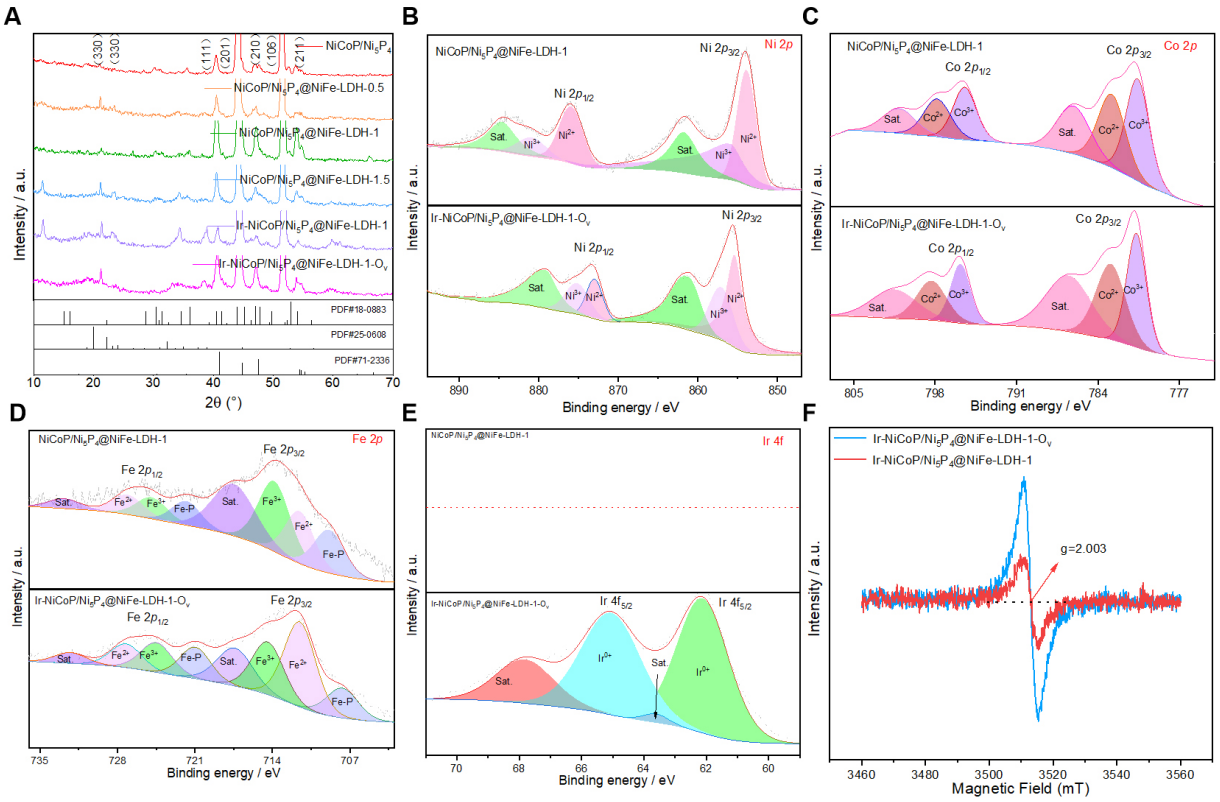

Figure 1. Structural characterization of Ir-NiCoP/Ni_5P_4@NiFe-LDH-1-O_V. (A) XRD. (B) XPS of Ni 2p; (C) Co 2p; (D) Fe 2p; (E) Ir 4f; (F) EPR of the samples. EPR: Electron paramagnetic resonance; XRD: X-ray diffraction; LDH: layered double hydroxide; XPS: X-ray photoelectron spectroscopy.

Supplementary Figure 4, Figure 2D and E show a low-magnification TEM image and high-resolution TEM (HRTEM) images of the as-prepared NiCoP/Ni_5P_4@NiFe-LDH-1 and Ir-NiCoP/Ni_5P_4@NiFe-LDH-1-O_V. For NiCoP/Ni_5P_4@NiFe-LDH-1 [Supplementary Figure 4], lattice spacings of 0.2268 nm and 0.1658 nm are indexed to the Ni_5P_4 (210) and NiCoP (211) planes, respectively, indicating the presence of both phases and high sample purity[30]. In the Ir-doped, $NaBH_4$-treated sample [Figure 2D and E], the corresponding spacings are 0.2248 nm for Ni_5P_4 (210) and 0.1603 nm for NiCoP (211), representing changes of 0.0020 and 0.0055 nm, respectively, relative to NiCoP/Ni_5P_4@NiFe-LDH-1. These observations, consistent with XRD results, further substantiate successful Ir incorporation. The selected area electron diffraction (SAED) pattern further reveals distinct diffraction rings attributable to NiCoP, which can be indexed to the lattice spacings of the (210), (111), (201), and (211) crystallographic planes [Figure 2F]. To further confirm the elemental distribution in the synthesized Ir-NiCoP/Ni_5P_4@NiFe-LDH-1-O_V-1, energy-dispersive X-ray spectroscopy (EDS) mapping was performed [Figure 2G]. The maps reveal uniform distributions of Ni, Co, P, Fe, and Ir across the material, supporting successful synthesis and homogeneous incorporation of all constituent elements.

The electrocatalytic performance of all synthesized samples was evaluated in a three-electrode configuration using an alkaline electrolyte (1 M KOH). Figure 3A presents the linear sweep voltammetry (LSV) curves for HER at a scan rate of 5 mV s^{-1}. The results demonstrate that Ir-NiCoP/Ni_5P_4@NiFe-LDH-1-O_V samples exhibit a significantly lower overpotential compared to all other catalysts, indicating superior HER activity. A systematic comparison of overpotentials at the various current densities (-10, -50, and -100 mA cm^{-2}) is presented in Supplementary Figure 5. Among all catalysts, Ir-NiCoP/Ni_5P_4@NiFe-LDH-1-O_V exhibits superior performance with the lowest overpotentials of 52.7, 106.7, and 154.7 mV, respectively. This

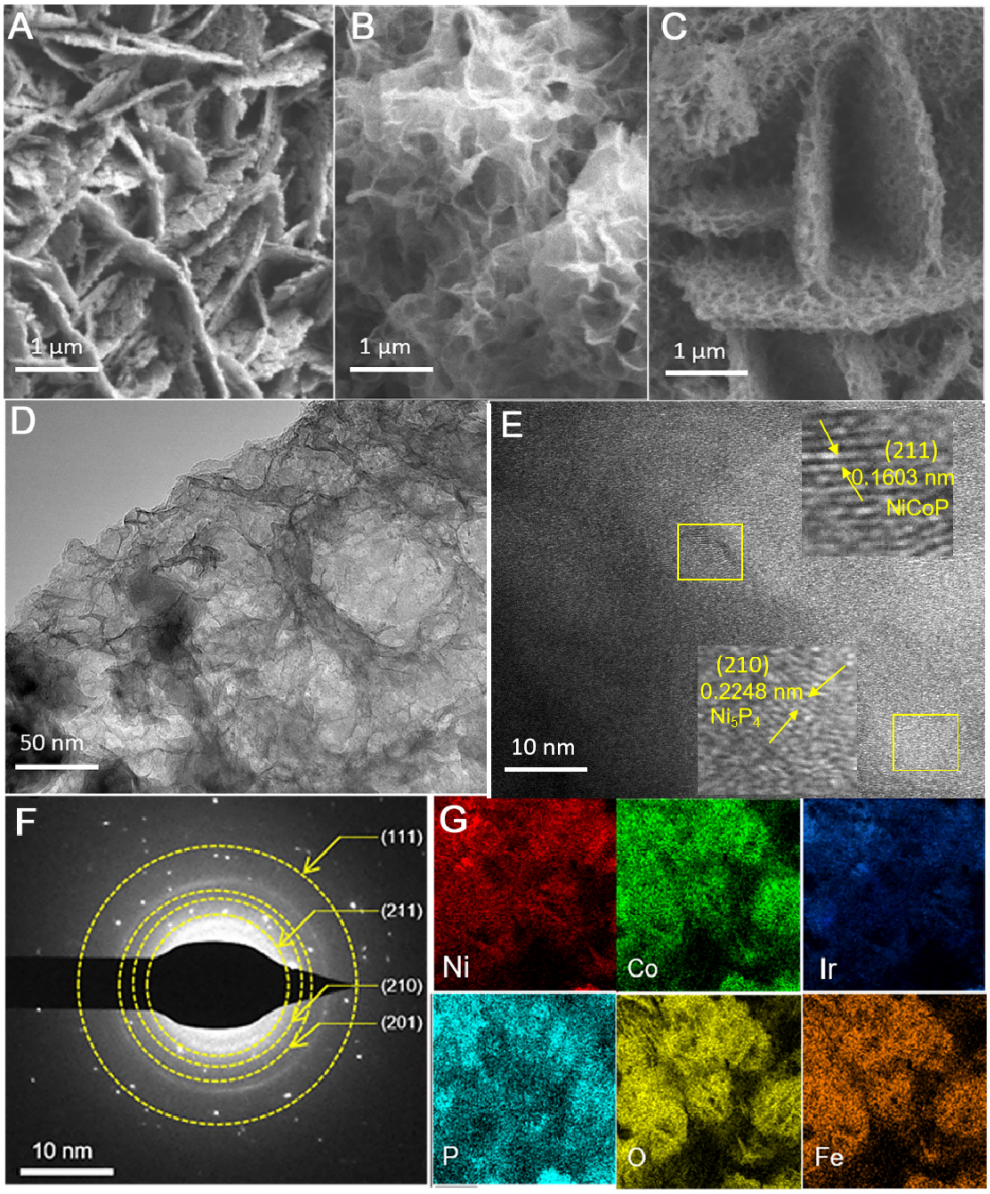

Figure 2. Morphology of the prepared samples. (A) SEM image of NiCoP/Ni_5P_4@NiFe-LDH-1; (B) SEM image of Ir-NiCoP/Ni_5P_4@NiFe-LDH-1; (C) SEM image of Ir-NiCoP/Ni_5P_4@NiFe-LDH-1-O_V; (D) TEM image of Ir-NiCoP/Ni5P4@NiFe-LDH-1-O_V; (E) HRTEM image; (F) SAED pattern of Ir-NiCoP/Ni_5P_4@NiFe-LDH-1-O_V; (G) Elemental mapping of Ir-NiCoP/Ni_5P_4@NiFe-LDH-1-O_V. SEM: Scanning electron microscopy; LDH: layered double hydroxide; TEM: transmission electron microscopy; HRTEM: high-resolution TEM; SAED: selected area electron diffraction.

represents a notable enhancement compared to Ir-NiCoP/Ni_5P_4@NiFe-LDH-1 (62.7, 127.7, and 182.7 mV) and substantially surpasses all reference materials. The marked improvement following $NaBH_4$ reduction validates the efficacy of oxygen vacancy introduction as a strategy for enhancing electrocatalytic performance[31]. Tafel slopes were extracted from the LSV curves [Figure 3B]. The values are 96.77, 110.39, 96.18, 92.70, and 74.09 mV dec^{-1}. Among these, Ir-NiCoP/Ni_5P_4@NiFe-LDH-1-O_V shows the smallest slope, indicating faster HER kinetics[32]. Double-layer capacitances (C_{dl}) were extracted from the linear dependence of capacitive current on scan rate [Figure 3C], yielding values of 0.0112, 0.0251, 0.0068, 0.0331, 0.0306, and 0.0487 mF cm^{-2} for the above catalysts. Notably, Ir-NiCoP/Ni_5P_4@NiFe-LDH-1-O_V exhibits the highest C_{dl}, indicating a substantially enlarged electrochemically active surface area (ECSA). This enhanced ECSA is attributed to the synergistic effects of Ir doping and oxygen vacancy engineering via $NaBH_4$ treatment, which collectively increase both the density and accessibility of catalytically active sites for HER.

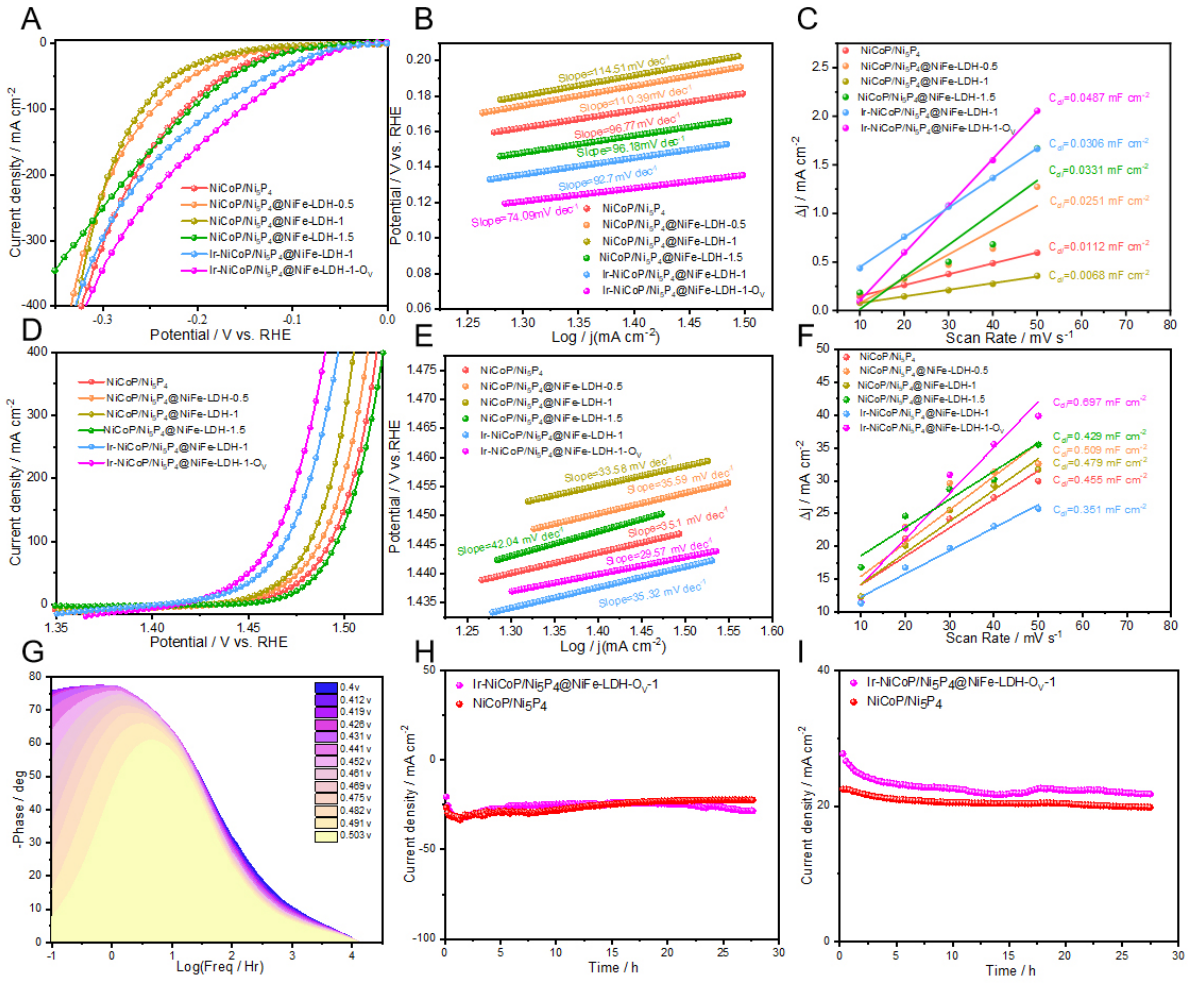

Figure 3. HER and OER performance of the samples in 1 M KOH. (A) LSV curves in HER; (B) Tafel plots in HER; (C) C_{dl} value; (D) LSV curves in OER; (E) Tafel plots in OER; (F) C_{dl} value; (G) Bode diagram; (H) Chronoamperometric stability tests (HER); (I) Chronoamperometric stability tests (OER). LSV: Linear sweep voltammetry.

The OER activity of the as-synthesized materials was evaluated in a three-electrode electrochemical cell. The electrocatalytic performance was investigated in 1 M KOH electrolyte at a scan rate of 2 mV s^{-1}. Figure 3D presents LSV curves of the materials. Among all the materials examined, Ir-NiCoP/Ni_5P_4@NiFe-LDH-1-O_V exhibited the lowest overpotential, demonstrating superior OER activity compared to the other catalysts. To provide a more intuitive comparison, Supplementary Figure 6 displays the overpotentials required to achieve current densities of 10, 50, and 100 mA cm^{-2}. Among all tested materials, Ir-NiCoP/Ni_5P_4@NiFe-LDH-1-O_V exhibited the lowest overpotentials of 197.3, 220.3, and 232.3 mV at 10, 50, and 100 mA cm^{-2}, respectively. These values are substantially lower than those of the other five materials, confirming its superior OER catalytic performance. Tafel analysis [Figure 3E] yields slopes of 35.1, 35.59, 33.58, 42.04, 35.32, and 29.57 mV dec^{-1} for the as-prepared NiCoP/Ni_5P_4, NiCoP/Ni_5P_4@NiFe-LDH-0.5, NiCoP/Ni_5P_4@NiFe-LDH-1, NiCoP/Ni_5P_4@NiFe-LDH-1.5, Ir-NiCoP/Ni_5P_4@NiFe-LDH-1, and Ir-NiCoP/Ni_5P_4@NiFe-LDH-1-O_V, respectively, implying the most favorable apparent kinetics. C_{dl} derived from cyclic voltammetry [Figure 3F] are 0.455, 0.509, 0.479, 0.429, 0.351, and 0.697 mF cm^{-2} for the same series, indicating that Ir-NiCoP/Ni_5P_4@NiFe-LDH-1-O_V shows the largest electrochemically active surface area and the highest density of accessible sites. Figure 3G displays the Bode plot of Ir-NiCoP/Ni_5P_4@NiFe-LDH-1-O_V, where the phase angle progressively decreases as the applied potential increases from 0.4 V to 0.503 V, indicating enhanced electron transfer kinetics. Particularly at higher potentials (0.503 V), the significantly reduced

phase angle indicates accelerated electron transfer, which facilitates the catalytic reaction process. To comprehensively evaluate the electrocatalytic performance, radar charts were constructed [Supplementary Figure 7], comparing the overpotentials at 10 mA cm^{-2}, Tafel slopes, and C_{dl} for both HER and OER across all materials. The radar plot clearly demonstrates that Ir-NiCoP/Ni_5P_4@NiFe-LDH-1-O_V outperforms the other five catalysts across all evaluated metrics. Electrochemical impedance spectroscopy [Supplementary Figure 8] further shows the smallest semicircle and a Nyquist plot closest to the origin for Ir-NiCoP/Ni_5P_4@NiFe-LDH-1-O_V, indicating the lowest charge-transfer resistance and the most rapid charge transport, consistent with its lower OER overpotentials. Finally, constant potential durability tests for both HER and OER [Figure 3H and I] show that Ir-NiCoP/Ni_5P_4@NiFe-LDH-1-O_V maintains superior activity for approximately 28 h compared to NiCoP/Ni_5P_4, confirming its robust operational stability. To further demonstrate the material's competitiveness, its properties were compared with those of commercial and recently reported state-of-the-art catalysts [Supplementary Table 1], highlighting its excellent performance.

To elucidate the surface evolution during catalysis, XPS spectra were acquired for Ir-NiCoP/Ni_5P_4@NiFe-LDH-O_V-1 before and after prolonged OER operation in an alkaline electrolyte. The spectral changes are consistent with OER-induced surface reconstruction, revealing substantial alterations in the near-surface chemical environment and the *in situ* generation of catalytically active sites that are absent in the as-prepared material[33,34]. As shown in Figure 4A, $NaBH_4$ pretreatment has a negligible effect on the intrinsic electronic states: the binding energies of the constituent elements remain essentially unchanged, indicating that the composition and stability are preserved. Following OER cycling, significant binding energy shifts are observed across multiple metal centers. The Ni^{3+} $2p_{1/2}$ peak shifts by 2.1 eV toward lower binding energy[34], while the Co^{2+} $2p_{1/2}$ peak exhibits a more pronounced 2.8 eV negative shift [Figure 4B]. In contrast, Fe displays negligible variation [Figure 4C], suggesting relative chemical stability under OER conditions[35]. Notably, the Ir $4f_{7/2}$ component undergoes a 0.30 eV downshift [Figure 4D]. These systematic negative binding energy shifts for Ni, Co, and Ir provide compelling evidence of extensive surface reconstruction accompanied by charge redistribution during electrochemical activation[36]. The distinct electronic perturbations, particularly involving Ir, underscore its pivotal role in modulating the local electronic structure and thereby enhancing the electrode's electrocatalytic performance. As shown in Figure 4E and F, the O 1s and P 2p spectra exhibit no discernible changes, indicating that the oxygen- and phosphorus-related chemical environments remain largely unchanged during the process. The binding energies of metal centers (Ni, Co, Ir) exhibit pronounced negative shifts, whereas the O 1s and P 2p peak positions remain virtually unchanged. The negative shift of metal 2p peaks is attributed to the decreased oxidation states of metal centers during the OER process. The invariant O 1s peak position arises from the dynamic equilibrium established among lattice oxygen, surface hydroxyl groups, and adsorbed oxygen species. More significantly, the stability of P 2p peaks substantiates the effective protective role of the outer NiFe-LDH layer in shielding the phosphide core from electrochemical oxidation. From the TEM images, it is clear that after electrochemical cycling [Figure 4G], the Ir-NiCoP/Ni_5P_4@NiFe-LDH-1-O_V sample retains its nanosheet morphology, indicating high structural stability of the catalyst. As shown in the HRTEM images [Figure 4H], lattice fringes with spacings of 0.1908 and 0.2260 nm can be indexed to the (211) plane of NiCoP and the (210) plane of Ni_5P_4, respectively, revealing a pronounced increase in lattice spacing after cycling.

To evaluate the performance of the synthesized catalyst, a two-electrode overall water splitting (OWS) cell was assembled, using the as-prepared material as both anode and cathode [Figure 5A]. The LSV curves [Figure 5B] show that current densities of 10 and 50 mA cm^{-2} are achieved at cell voltages of 1.35 and 1.74 V, respectively. After cycling, the required voltages increased only slightly to 1.42 and 1.80 V, indicating minimal performance decay. The overall cell architecture remains intact and the OWS activity is largely preserved. Faradaic efficiency (FE) was quantified by collecting H_2 and O_2 generated during electrolysis in a

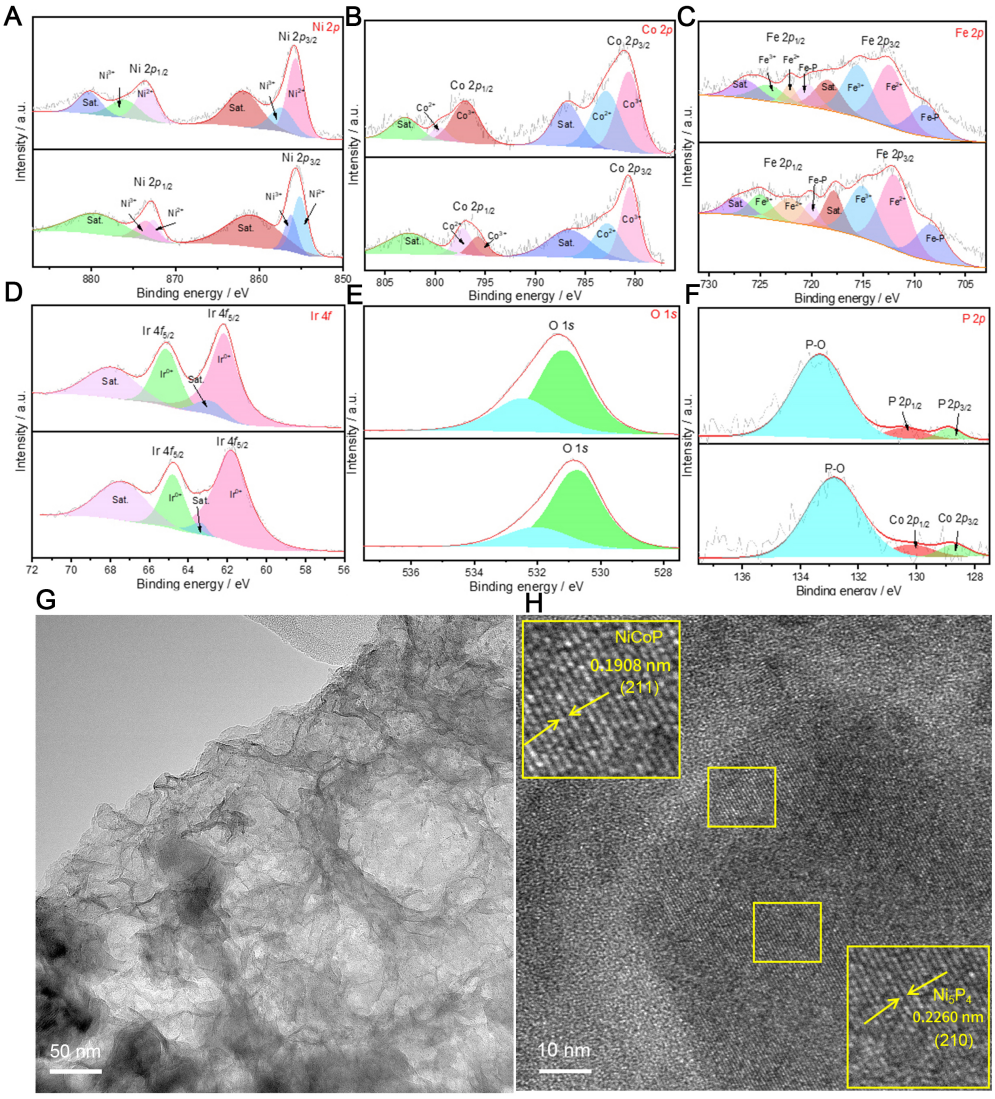

Figure 4. Structural characterization of Ir-NiCoP/Ni_5P_4@NiFe-LDH-1-O_V before and after electrochemical cycling. (A) XPS of Ni 2p; (B) Co 2p; (C) Fe 2p; (D) Ir 4f; (E) O 1s; (F) P 2p; (G) TEM image of Ir-NiCoP/Ni_5P_4@NiFe-LDH-1-O_V after electrochemical cycling; (H) HRTEM image. LDH: Layered double hydroxide; XPS: X-ray photoelectron spectroscopy; TEM: transmission electron microscopy; HRTEM: high-resolution TEM.

symmetric Ir-NiCoP/Ni_5P_4@NiFe-LDH-1-O_V. Ir-NiCoP/Ni_5P_4@NiFe-LDH-1-O_V cell using the water-displacement method. The gas volume-time plots [Figure 5C] show an H_2:O_2 volume ratio of ~2:1, in excellent agreement with water splitting stoichiometry, indicating an FE approaching 100%. Continuous electrolysis for 100 h further demonstrates the durability of Ir-NiCoP/Ni_5P_4@NiFe-LDH-1-O_V [Figure 5D]. The post-cycling SEM inset reveals slight surface roughening, consistent with reconstruction during long-term electrolysis.

To explore this potential, the performance of Ir-NiCoP/Ni_5P_4@NiFe-LDH-1-O_V was evaluated in an ammoniacal alkaline electrolyte (1 M KOH + NH_3·H_2O). This medium, which combines KOH with aqueous ammonia, provides a favorable environment for AOR while maintaining high ionic conductivity. Regarding selectivity, under the operating conditions employed in this work, ammonia molecules are preferentially oxidized at the catalyst surface in the alkaline ammonia solution, making AOR the dominant anodic reaction rather than OER. Furthermore, the theoretical potential of AOR is only -0.06 V *vs.* RHE (under alkaline

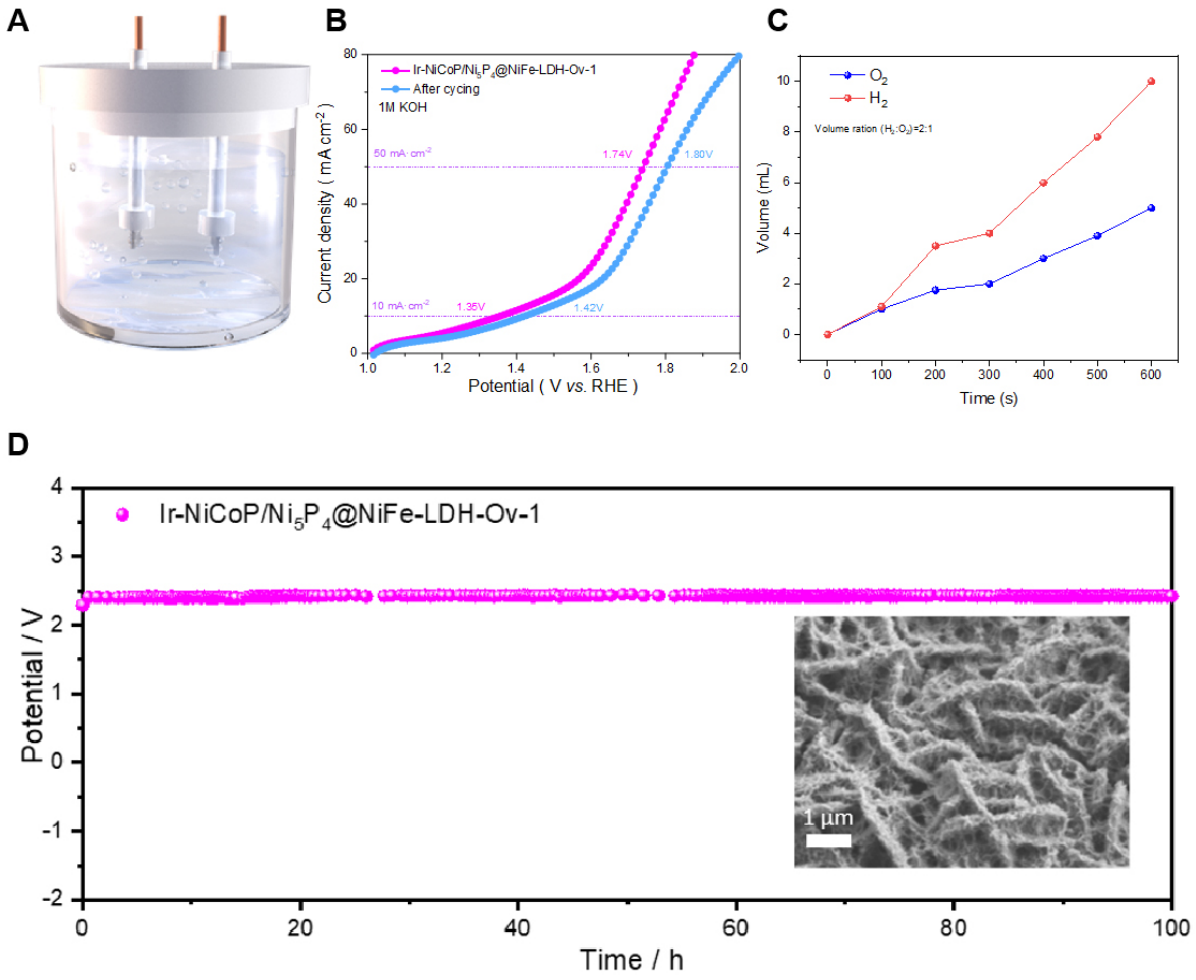

Figure 5. Overall water splitting performance of samples and Faraday efficiency test. (A) Schematic of the overall water splitting device; (B) LSV curves; (C) Faradaic efficiency curve; (D) Chronoamperometric stability tests. LSV: Linear sweep voltammetry; LDH: layered double hydroxide.

conditions), which is significantly lower than that of OER (1.23 V *vs.* RHE), thereby substantially reducing the overall cell voltage and improving energy efficiency[36,37]. Electrochemical testing in this electrolyte enables a comprehensive assessment of catalytic activity, stability, and selectivity, generating essential data to guide optimization of ammonia-enabled hydrogen production. In summary, the combination of low thermodynamic energy demand, environmental compatibility, and high hydrogen-storage capacity makes ammonia electrolysis a compelling research direction. With continued advances in catalyst design and electrolyte engineering, ammonia electrolysis could assume a pivotal role in the hydrogen value chain, accelerating the hydrogen economy and offering practical pathways to address hydrogen storage and transport.

For HER evaluation, Figure 6A presents the LSV curves of all materials. The catalysts (Ir-NiCoP/Ni_5P_4@NiFe-LDH-1 and Ir-NiCoP/Ni_5P_4@NiFe-LDH-1-O_V) exhibit significantly lower overpotentials compared to the other materials. Among these, Ir-NiCoP/Ni_5P_4@NiFe-LDH-1-O_V demonstrates superior performance compared with Ir-NiCoP/Ni_5P_4@NiFe-LDH-1, consistent with results obtained from alkaline water electrolysis, further confirming the beneficial effect of $NaBH_4$ treatment on enhancing electrocatalytic activity. Supplementary Figure 9 provides a quantitative comparison of overpotentials at current densities of -10, -50, and -100 mA cm^{-2}. The baseline materials show relatively high

overpotentials. In contrast, Ir-NiCoP/Ni_5P_4@NiFe-LDH-1-O_V achieves remarkably low overpotentials of 72.7, 132.7, and 188.7 mV at -10, -50, and -100 mA cm^{-2}, respectively. These values represent further improvements compared to Ir-NiCoP/Ni_5P_4@NiFe-LDH-1 (76.7, 138.7, and 188.7 mV), unambiguously demonstrating that $NaBH_4$ treatment substantially enhances the catalytic performance. To further probe reaction kinetics, Tafel slopes were derived from Tafel plots constructed from the LSV data [Figure 6B]. Ir-NiCoP/Ni_5P_4@NiFe-LDH-1-O_V shows a Tafel slope of 96.44 mV dec^{-1}, smaller than those of NiCoP/Ni_5P_4 (128.55 mV dec^{-1}), NiCoP/Ni_5P_4@NiFe-LDH-0.5 (138.95 mV dec^{-1}), NiCoP/Ni_5P_4@NiFe-LDH-1 (130.85 mV dec^{-1}), and NiCoP/Ni_5P_4@NiFe-LDH-1.5 (131.79 mV dec^{-1}). Compared with Ir-NiCoP/Ni_5P_4@NiFe-LDH-1, however, the O_V-1 sample exhibits a slightly higher slope, possibly reflecting electrolyte-specific effects in ammoniacal media. Capacitive measurements corroborate these trends: C_{dl} of Ir-NiCoP/Ni_5P_4@NiFe-LDH-1-O_V is 0.187 mF cm^{-2} [Figure 6C], exceeding those of NiCoP/Ni_5P_4 (0.045 mF cm^{-2}), NiCoP/Ni_5P_4@NiFe-LDH-0.5 (0.062 mF cm^{-2}), NiCoP/Ni_5P_4@NiFe-LDH-1 (0.016 mF cm^{-2}), NiCoP/Ni5P4@NiFe-LDH-1.5 (0.055 mF cm^{-2}), and Ir-NiCoP/Ni_5P_4@NiFe-LDH-1 (0.155 mF cm^{-2}). The larger C_{dl} implies a greater ECSA and a higher density of accessible active sites for Ir-NiCoP/Ni_5P_4@NiFe-LDH-1-O_V, consistent with enhanced apparent kinetics. The AOR performance of the samples was further investigated under identical conditions, with results presented in Figure 6D-F. Figure 6D displays the LSV curves for all materials, revealing that Ir-NiCoP/Ni_5P_4@NiFe-LDH-1-O_V exhibits significantly lower overpotentials compared to the other five catalysts. A detailed quantitative analysis is shown in Supplementary Figure 10. Ir-NiCoP/Ni_5P_4@NiFe-LDH-1-O_V achieves overpotentials of 101.3, 148.3, and 197.3 mV at current densities of 10, 50, and 100 mA cm^{-2}, respectively. These values demonstrate superior performance compared to Ir-NiCoP/Ni_5P_4@NiFe-LDH-1 (101.3, 168.3, and 215.3 mV at the same current densities), with particularly notable improvements at higher current densities. When benchmarked against the remaining materials - NiCoP/Ni_5P_4 (111.3, 193.3, and 229.3 mV), NiCoP/Ni_5P_4@NiFe-LDH-0.5 (131.3, 197.3, and 231.3 mV), NiCoP/Ni_5P_4@NiFe-LDH-1 (123.3, 216.3, and 235.3 mV), and NiCoP/Ni_5P_4@NiFe-LDH-1.5 (117.3, 196.3, and 237.3 mV) - Ir-NiCoP/Ni_5P_4@NiFe-LDH-1-O_V consistently shows substantially reduced overpotentials across all tested current densities. Corresponding Tafel slopes [Figure 6E] are 118.72, 106.49, 128.28, 111.04, 101.48 mV dec^{-1} for the sequence of samples, indicating more favorable apparent kinetics for O_V-1 even after replacing KOH with $NH_3 \cdot H_2O$. From cyclic voltammetry measurements, the C_{dl} [Figure 6F] are 0.489, 0.291, 0.421, 0.257, 0.564, and 0.657 mF cm^{-2}, respectively, with O_V-1 exhibiting the largest value. This result is consistent with a larger electrochemically active surface area and a higher density of accessible active sites after Ir incorporation and $NaBH_4$ treatment. Electrochemical impedance spectroscopy (EIS) data are shown in Figure 6G. The semicircle diameter observed in the high-frequency region represents the charge transfer resistance (R_{ct}) at the electrode-electrolyte interface. The notably smaller semicircle for Ir-NiCoP/Ni_5P_4@NiFe-LDH-1-O_V indicates markedly reduced R_{ct}, demonstrating accelerated interfacial charge transfer kinetics and enhanced electronic conductivity that underpin its outstanding electrocatalytic activity. To comprehensively assess the electrocatalytic performance, radar charts comparing overpotentials at 10 mA cm^{-2}, Tafel slopes, and C_{dl} for both HER and AOR were constructed [Supplementary Figure 11]. These plots clearly demonstrate that Ir-NiCoP/Ni_5P_4@NiFe-LDH-1-O_V consistently outperforms the other five materials across all evaluated metrics. Finally, constant potential durability tests for HER and AOR in the ammoniacal electrolyte [Figure 6H and I] show that Ir-NiCoP/Ni_5P_4@NiFe-LDH-1-O_V maintains superior activity for approximately 28 h relative to NiCoP/Ni_5P_4, demonstrating robust operational stability.

Further analysis shows that Ir-NiCoP/Ni_5P_4@NiFe-LDH-1-O_V exhibits excellent activity for water electrolysis. Its engineered architecture and optimally distributed active sites accelerate charge-transfer kinetics while lowering the overpotential. Consequently, water splitting proceeds efficiently with reduced energy input, and the catalyst maintains stability during prolonged operation. Together, these results

establish Ir-NiCoP/Ni_5P_4@NiFe-LDH-1-O_V as a high-performance water-electrolysis catalyst with broad

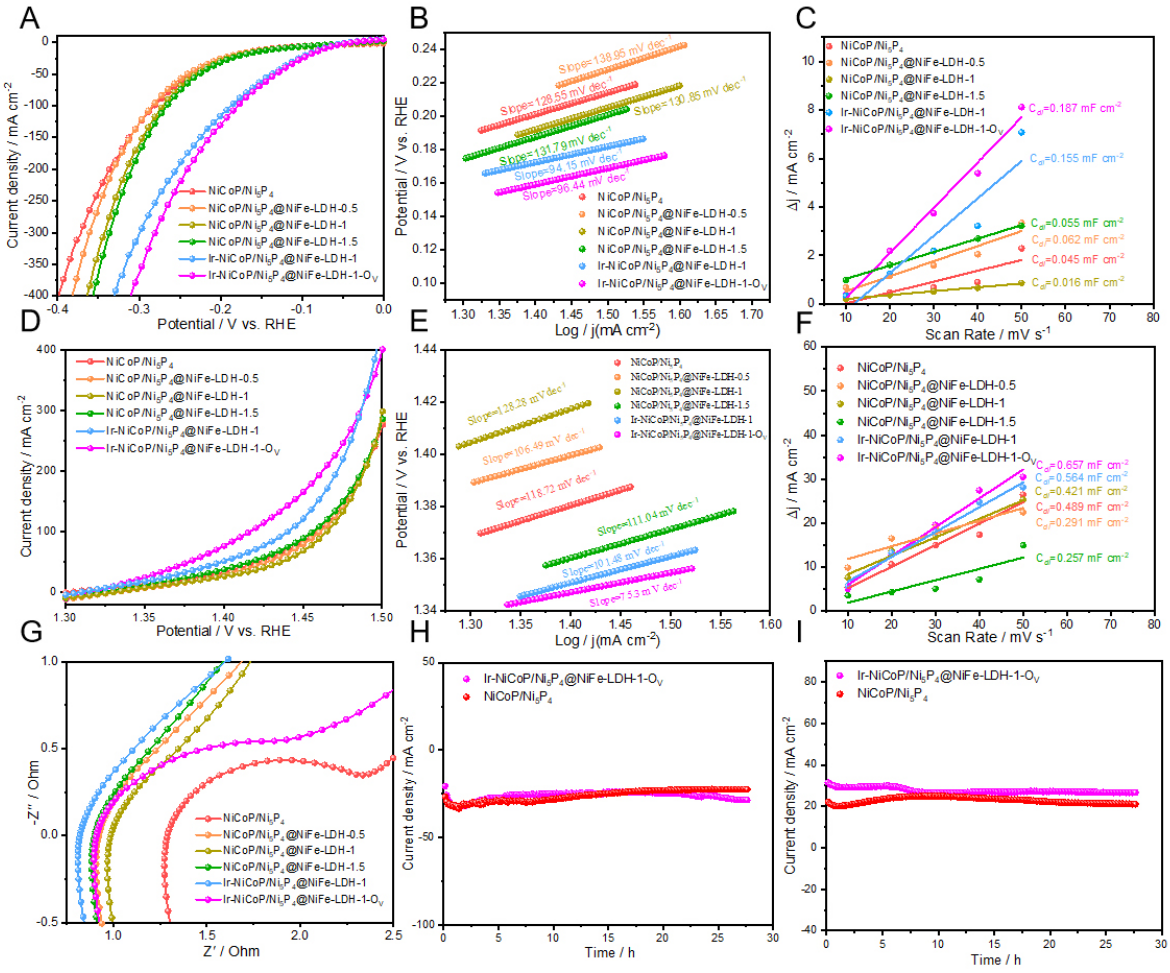

Figure 6. HER and AOR performance of the samples in 1 M KOH + $NH_3 \cdot H_2O$. (A) LSV curves, (B) Tafel plots, and (C) C_{dl} value of HER; (D) LSV curves, (E) Tafel plots, (F) C_{dl} value, and (G) EIS curves of AOR; (H) Chronoamperometric stability tests of HER; (I) Chronoamperometric stability tests of AOR. HER: Hydrogen evolution reaction; AOR: ammonia oxidation reaction; LSV: linear sweep voltammetry; EIS: electrochemical impedance spectroscopy.

application potential. The combination of high energy conversion efficiency and durability provides a robust technological basis for hydrogen production by water splitting in the clean energy sector. This work not only provides an experimental foundation for developing efficient, low-cost electrocatalysts, but also suggests new avenues for the sustainable growth of the hydrogen energy value chain.

CONCLUSION

In summary, we successfully prepared Ir-doped NiCoP/Ni_5P_4@NiFe-LDH composite materials through a facile two-step hydrothermal method. Following $NaBH_4$ treatment, the Ir-NiCoP/Ni_5P_4@NiFe-LDH-1-O_V material achieved 10 mA cm^{-2} at an overpotential of 52.7 mV for HER in 1 M KOH electrolyte. The catalyst retained its activity after 28 h of continuous cycling, indicating robust durability. In the two-electrode electrolyzer configuration, the catalyst achieved a remarkably low cell voltage for overall water splitting and maintained stable operation for 100 h without performance degradation. Furthermore, in $NH_3 \cdot H_2O$ + 1 M KOH electrolyte, the catalyst exhibited an exceptionally low overpotential of only 72.7 mV at a current

density of 10 mA cm^{-2}. This work provides valuable insights into the rational design of advanced multifunctional electrocatalysts.

DECLARATIONS

Authors' contributions

Conceptualization, data curation, writing - original draft: Zhao, Z.; Sui, L.
Data curation, figure design: Wang, Z.; Song, S.; Wang, J.; Li, Y.
Writing - review and editing, funding acquisition, supervision: Zhao, D.; Li, G.; Miao, L.

Availability of data and materials

The raw data supporting the conclusions of this article will be made available by the corresponding author upon reasonable request.

AI and AI-assisted tools statement

Not applicable.

Financial support and sponsorship

This project was supported by the College Student Innovation and Entrepreneurship Project (S202410164017).

Conflicts of interest

All authors declared that there are no conflicts of interest.

Ethical approval and consent to participate

Not applicable.

Consent for publication

Not applicable.

Copyright

© The Author(s) 2026.

Supplementary Materials

Supplementary Materials

REFERENCES

1. Pu, T.; Ding, J.; Zhang, F.; et al. Dual atom catalysts for energy and environmental applications. *Angew. Chem. Int. Ed.* **2023**, *62*, e202305964. DOI PubMed
2. Cao, P.; Liu, Y.; Zhang, Q.; Guo, C.; Li, J.; Zeng, Q. MXene/MOF composites: synergistic platforms for advanced Energy, catalysis, and environmental applications. *Coord. Chem. Rev.* **2025**, *545*, 217018. DOI
3. Zhou, H.; Xu, S.; Zhang, B.; et al. *In situ* reconstructed amorphous MOOH-enhanced NiCoP@NiFe-LDH bifunctional electrocatalyst for long durable seawater electrolysis. *Inorg. Chem. Front.* **2026**, *13*, 666-79. DOI
4. Johnson, N.; Liebreich, M.; Kammen, D. M.; Ekins, P.; Mckenna, R.; Staffell, I. Realistic roles for hydrogen in the future energy transition. *Nat. Rev. Clean. Technol.* **2025**, *1*, 351-71. DOI
5. Zhang, L.; Qi, F.; Ren, R.; et al. Recent advances in green hydrogen production by electrolyzing water with anion-exchange membrane. *Research* **2025**, *8*, 0677. DOI PubMed PMC
6. Mao, J.; Liang, J.; Li, Y.; et al. Electrochemical lithiation regulates the active hydrogen supply on Ru-Sn nanowires for hydrogen evolution toward the high-performing anion exchange membrane water electrolyzer. *J. Am. Chem. Soc.* **2025**, *147*, 7711-20. DOI
7. Zhang, X.; Cao, C.; Ling, T.; Ye, C.; Lu, J.; Shan, J. Developing practical catalysts for high-current-density water electrolysis. *Adv. Energy. Mater.* **2024**, *14*, 2402633. DOI
8. Gao, X.; Chen, Y.; Wang, Y.; et al. Next-generation green hydrogen: progress and perspective from electricity, catalyst to electrolyte in electrocatalytic water splitting. *Nano. Micro. Lett.* **2024**, *16*, 237. DOI PubMed PMC
9. Cao, L.; Zhang, J.; Ding, L.; Du, Z.; He, C. Metal-organic frameworks derived transition metal phosphides for electrocatalytic water splitting. *J. Energy. Chem.* **2022**, *68*, 494-520. DOI

10. Geng, P.; Ji, B.; Guo, Y.; Xiao, C.; Wan, J.; Li, C. M. MOF-derived transition metal phosphides for rechargeable batteries. *Chem. Eng. J.* **2025**, *516*, 164033. DOI
11. Zhou, Z.; Shi, X.; Yin, J.; Kong, W.; Sun, J.; Wen, Z. Symbiotic growth of cobalt phosphides facilitates multiphase synergic function on long-cycling stability. *Chem. Phys. Lett.* **2020**, *749*, 137403. DOI
12. Gao, Z.; Gao, Q.; Liu, Z.; et al. High-efficiency hydrogen evolution reaction catalyzed by iron phosphide nanocrystals. *RSC. Adv.* **2016**, *6*, 114430-5. DOI
13. Song, L.; Zhang, S. A versatile route to synthesizing bulk and supported nickel phosphides by thermal treatment of a mechanical mixing of nickel chloride and sodium hypophosphite. *Powder. Technol.* **2011**, *208*, 713-6. DOI
14. Tang, D.; Li, T.; Li, C. M. Metal and phosphonium-based ionic liquid: a new Co and P dual-source for synthesis of cobalt phosphide toward hydrogen evolution reaction. *Int. J. Hydrogen. Energy.* **2019**, *44*, 1720-6. DOI
15. Galindo-ortega, Y.; Infantes-molina, A.; Huirache-acuña, R.; et al. Active ruthenium phosphide as selective sulfur removal catalyst of gasoline model compounds. *Fuel. Process. Technol.* **2020**, *208*, 106507. DOI
16. Liu, D.; Ai, H.; Chen, M.; et al. Multi-phase heterostructure of CoNiP/Co_xP for enhanced hydrogen evolution under alkaline and seawater conditions by promoting H_2O dissociation. *Small* **2021**, *17*, e2007557. DOI
17. Wu, L.; Yu, L.; Mcelhenny, B.; et al. Rational design of core-shell-structured CoP_x@FeOOH for efficient seawater electrolysis. *Appl. Catal. B. Environ.* **2021**, *294*, 120256. DOI
18. Liu, Y.; Hu, H.; Wang, K.; Huang, J.; Wang, D. Advancing seawater electrolysis: NiFe-LDH-based electrocatalysts for the oxygen evolution reaction. *Adv. Energy. Mater.* **2025**, *16*, e04101. DOI
19. Li, J.; Naren, G.; Tang, C.; et al. Asymmetric ruthenium-iron dipole enabling fast alkaline water splitting on ruthenium-doped iron-nickel layered double hydroxides. *Mater. Rep. Energy.* **2025**, *5*, 100359. DOI
20. Abdelghafar, F.; Xu, X.; Guan, D.; et al. New nanocomposites derived from cation-nonstoichiometric Ba_x(Co, Fe, Zr, Y)$O_{3-\delta}$ as efficient electrocatalysts for water oxidation in alkaline solution. *ACS. Mater. Lett.* **2024**, *6*, 2985-94. DOI
21. Fan, M.; Cui, J.; Wu, J.; Vajtai, R.; Sun, D.; Ajayan, P. M. Improving the catalytic activity of carbon-supported single atom catalysts by polynary metal or heteroatom doping. *Small* **2020**, *16*, e1906782. DOI
22. Wang, S.; Chen, Z.; Sun, L.; et al. Synergistic mechanism of disparate surface hydroxyls and oxygen vacancies towards peroxymonosulfate activation for durable water decontamination. *Chem. Eng. J.* **2025**, *503*, 158259. DOI
23. Xue, N.; Lin, Z.; Li, P.; Diao, P.; Zhang, Q. Sulfur-doped $CoSe_2$ porous nanosheets as efficient electrocatalysts for the hydrogen evolution reaction. *ACS. Appl. Mater. Interfaces.* **2020**, *12*, 28288-97. DOI PubMed
24. Yang, Y.; Hao, J.; Lyu, C.; et al. Electron islands-induced interface engineering in FeP@NiCoP/Mo_4P_3 for efficient hydrogen evolution catalysis. *Adv. Funct. Mater.* **2025**, *35*, 2507225. DOI
25. Sial, M. A. Z. G.; Liu, S.; Zou, J.; et al. NiCoFe alloy multishell hollow spheres with lattice distortion to trigger efficient hydrogen evolution in acidic medium. *Sustain. Energy. Fuels.* **2019**, *3*, 3310-7. DOI
26. Li, X.; Wu, T.; Li, N.; et al. Vertically staggered porous Ni_2P/Fe_2P nanosheets with trace Ru doping as bifunctional electrocatalyst for alkaline seawater splitting. *Adv. Funct. Mater.* **2024**, *34*, 2400734. DOI
27. Gao, L.; Yang, Z.; Sun, T.; et al. Autocatalytic surface reduction-assisted synthesis of PtW ultrathin alloy nanowires for highly efficient hydrogen evolution reaction. *Adv. Energy. Mater.* **2022**, *12*, 2103943. DOI
28. Su, P.; Huang, W.; Zhang, J.; et al. Fe atoms anchored on defective nitrogen doped hollow carbon spheres as efficient electrocatalysts for oxygen reduction reaction. *Nano. Res.* **2020**, *14*, 1069-77. DOI
29. Ma, F.; Chen, H.; Wu, H.; et al. Phase transition during sintering of layered transition metal oxide sodium cathodes. *Nano. Lett.* **2025**, *25*, 9293-301. DOI PubMed
30. Luo, J.; Deng, J.; Wang, H.; et al. High-performance FeCoNiMo bifunctional catalysts with hierarchical porosity for water splitting. *Tungsten* **2025**, *8*, 242-54. DOI
31. Zhang, P.; Wu, Q.; Wang, H.; et al. Z-scheme heterojunction $Zn_3(OH)_2(V_2O_7)(H_2O)_2$/V-Zn(O,S) for enhanced visible-light photocatalytic N_2 fixation via synergistic heterovalent vanadium states and oxygen vacancy defects. *Chin. J. Catal.* **2025**, *74*, 279-93. DOI
32. Ma, W.; Zhang, Y.; Wang, B.; et al. Significantly enhanced OER and HER performance of NiCo-LDH and NiCoP under industrial water splitting conditions through Ru and Mn bimetallic co-doping strategy. *Chem. Eng. J.* **2024**, *494*, 153212. DOI
33. Feng, J.; Wang, X.; Pan, H. In-situ reconstruction of catalyst in electrocatalysis. *Adv. Mater.* **2024**, *36*, e2411688. DOI
34. Wang, M.; Tan, H.; Liu, X.; Yan, X.; Liang, J. Energy and resource generation via electrochemical ammonia oxidation: from materials design to system integration. *Adv. Energy. Mater.* **2025**, *15*, e03846. DOI
35. Yu, T.; Tan, K.; Wu, J.; Zou, Y.; Yin, S. Bifunctional interstitial phosphorous doping strategy boosts platinum-zinc alloy for efficient ammonia oxidation reaction and hydrogen evolution reaction. *Nano. Res.* **2023**, *17*, 1182-9. DOI

36. Huan, Y.; He, Y.; Liu, S.; et al. Electrochemical ammonia oxidation reaction on nickel-based non-noble metal electrocatalysts: from mechanistic understanding to practical applications. *Adv. Energy. Mater.* **2025**, *15*, e03815. DOI
37. Du, L.; Xing, L.; Zhang, G.; Liu, X.; Rawach, D.; Sun, S. Engineering of electrocatalyst/electrolyte interface for ambient ammonia synthesis. *SusMat* **2021**, *1*, 150-73. DOI

Disclaimer/Publisher's Note: All statements, opinions, and data contained in this publication are solely those of the individual author(s) and contributor(s) and do not necessarily reflect those of OAE and/or the editor(s). OAE and/or the editor(s) disclaim any responsibility for harm to persons or property resulting from the use of any ideas, methods, instructions, or products mentioned in the content.

© The Author(s) 2026. Open Access This article is licensed under a Creative Commons Attribution 4.0 International License (https://creativecommons.org/licenses/by/4.0/), which permits unrestricted use, sharing, adaptation, distribution and reproduction in any medium or format, for any purpose, even commercially, as long as you give appropriate credit to the original author(s) and the source, provide a link to the Creative Commons license, and indicate if changes were made.